First-principles study of thermoelasticity and structural phase diagram of CaO

Pooja Vyas [1,*] A. B. Patel,[2] and N. K. Bhatt [1,†]

[1]*Department of Physics, Maharaja Krishnakumarsinhji Bhavnagar University, Bhavnagar 364001, Gujarat, India*

[2]*Department of Physics & Astronomy, Johns Hopkins University, 3400 N. Charles Street, Baltimore, Maryland 21218, USA*

(Received 26 September 2022; revised 9 January 2023; accepted 10 January 2023; published 23 January 2023)

We present pressure (P) and temperature (T) variations of elastic and anisotropic properties, solid-solid (rocksalt, B1 to cesium chloride, B2) and solid-liquid structural phase transitions of CaO. We employed first-principles density functional theory supplemented with an anharmonic contribution to phonon dynamics. Good agreement is obtained for all properties up to the pressure and temperature range relevant to the Earth's mantle and outer core. Born elastic criteria are generalized for arbitrary stress to elaborate the structural phase diagram from a thermoelastic viewpoint. We propose a self-consistent computational scheme to incorporate the effect of thermal hysteresis into Lindemann's melting law. This improvised melting law exhibits quantitative agreement with reported findings for the high-P melting curve. We find the triple point (i.e., the coexistence of B1, B2, and liquid phases) at 23 GPa and 4600 K. By examining the pressure-term included elastic properties, we can show that the solid-solid transition is mechanical in a pressure range of 0–200 GPa and temperature up to 3000 K. The softening of shear elastic constant C_{44} drives the B1-B2 phase transition. This assertion is corroborated by examining the phonon dispersion curve and mode Grüneisen parameter at different pressures for both B1 and B2 phases. The solid-liquid phase boundary can be treated accurately through the temperature-dependent thermodynamic Grüneisen parameter. Furthermore, in this paper, we predict a negative melting slope >140 GPa with a peak temperature of 7800 K, suggesting a smaller molar volume on the liquid side than that of the solid phase. This finding is supported by electronic band structure calculation. It is proposed that the hybridization of the empty $3d$ band of the cation with s orbitals lowers the conduction band to cross the Fermi energy at the Brillouin zone center and leads the insulator-to-metal/semimetal phase transition $\sim$200 GPa. Different electronic states on solid and liquid sides make the liquid phase more compressible than the solid phase, eventually reducing the melting temperature with pressure.

DOI: 10.1103/PhysRevB.107.014107

I. INTRODUCTION

Lime (CaO) is one of the important components in the Earth's lower mantle (LM) and upper mantle (UL), and it is believed that the region D″ at the bottom of the mantle is enriched in CaO [1]. The study of high-pressure structural phase transition (SPT) and elastic properties of lime and its usage in deriving calcium silicate perovskite $CaSiO_3$ (CaPv) from a geophysical viewpoint is vital for understanding the Earth's LM and outer core. For instance, thermal conductivity and mass transport mechanisms depend sensitively on the thermoelasticity and the structure [2]. The pressure (P) and temperature (T) across the LM and outer core span over 23 to $>$200 GPa at 2000 to $>$4000 K. As computed in this paper, this is the (P, T) region where the rocksalt (B1) structure with face-centered-cubic (fcc) space lattice, the cesium chloride (B2) structure with simple cubic space lattice, and the liquid phase have competing free energies. Transport across the rocky LM and the molten metallic core thus requires the knowledge of P, T variation of SPT and elasticity for these phases separately as well as at the onset of the phase transition. It is also essential to unveil the role played by the thermal stress at finite P, T conditions on elastic moduli and their connection in determining the high-P melting curve. It is noted that, in closely related compounds of the mantle, the anharmonic effect is also important. For instance, anharmonicity is detected in (i) the Raman spectrum of $MgSiO_3$ at ambient pressure [3], (ii) at the boundary across the olivine to wadsleyite transition [4], (iii) high-T stabilization of the cubic phase of CaPv [5], and (iv) in Mg orthoenstatite [6], to mention a few. Also, recent first-principles density functional theory (DFT)-based studies [7–16] on high-T thermal assessment of CaO have clearly shown the inadequacy of quasiharmonic approximation (QHA) above room temperature (RT). We [17] have thoroughly investigated the role of anharmonicity in reference to the projector augmented-wave (PAW) pseudopotential and the effect of exchange correlation (XC) on high-T thermodynamic properties for the B1 phase of CaO extending up to 3000 K. In this paper, we also discuss the bonding scenario in CaO at expanded volumes. In this conclusive paper, we suggest a non-negligible contribution due to phonon anharmonicity for CaO beyond RT, lesser for the local density approximation (LDA)+PAW scheme. Therefore, these studies advocate the need to calculate anharmonic phonon dynamics while deriving free energy for geophysical and geochemical exploration from a thermoelastic viewpoint.

*poojavyas1251995@gmail.com

†bhattnisarg@hotmail.com, nkb@mkbhavuni.edu.in

Experimentally, mimicking such an extreme environment to perform *in situ* measurement is challenging either due to grain size effects or the presence of impurities [18]. It is also difficult to obtain a single crystal for measuring the elastic properties, and thermal instability causes additional difficulties [19]. For instance, the phase transition from B1 to B2 in CaO has been observed from static diamond anvil cell and shock-wave measurements in a pressure range of 60–70 GPa [20–23]. Jeanloz and Ahrens [20] carried out a shock-wave study of the compression of CaO to 175 GPa, and they observed a phase transition from B1 to B2 at 60 GPa. However, the compression of the B2 phase was inadequately known from these shock-wave experiments, which exhibit an unusual dispersion >100 GPa. The authors attributed this dispersion to the thermally generated instabilities that would have resulted in another phase transition. The volume change at the B1-to-B2 transition and the compression of the B1 phase up to the transition pressure has also been determined statically in Refs. [21,22]. Richet *et al.* [23] reported the RT compression data to 135 GPa in a diamond anvil cell experiment. However, these studies exhibited the SPT only at RT, whereas a complete phase diagram is required for a better understanding of the behavior of the LM and the LM–Earth outer core interface.

Ab initio calculations provide an alternative to investigate SPT and thermoelastic response, and it is possible to deduce a complete structural phase diagram at an arbitrary point in the (P, T) plane. In these regards, the phase transition of CaO has also been studied theoretically but with a wide range of predicted phase transition pressures, ranging from 32 to 121 GPa [10,11,24–30]. The modified electron-gas study for CaO crystal by Cohen and Gordon [24] predicted the phase transition to be 121 GPa using the Watson function and 162 GPa using the Yamashita-Asano function. Mehl *et al.* [25] predicted the B1-B2 phase transition pressure using the potential-induced breathing to be 55 GPa. In another study, Mehl *et al.* [26], using the full-potential self-consistent linearized augmented plane-wave, showed the phase transition ∼54 GPa. Bukowinski [27] adopted the LDA, which resulted in transition pressure being 32 GPa, which was in better agreement with the experimental data [21]. The computations of Karki and Crain [29] based on DFT within LDA resulted in phase transition at 58 GPa. Phase transition at 56 GPa was also observed by Karki and Wentzcovitch [10] using a DFT-LDA-based investigation. Deng *et al.* [30] employed the *ab initio* plane-wave pseudopotential method and showed phase transition at 62.8 GPa. In a similar study, but using generalized gradient approximation (GGA), Jiang *et al.* [11] predicted the phase transition at 66.7 GPa. Although these studies show a wide scatter in SPT pressure at $T = 0$ K or RT, they reveal the specific trend in derived phase transition pressure. The LDA-based findings generally estimate smaller values for transition pressure than the GGA-based estimate. Similarly, even though the high-P analysis of the elastic behavior of lime can provide a better perception of elastic destabilization, very limited experimental findings are available, and virtually no experiments were attempted to examine the temperature effect on the pressure dependence of elastic moduli [31]. Oda *et al.* [32] have obtained T-dependent elastic constants (TDECs) but at ambient pressure. Several theoretical estimates for elastic constants (ECs) at high-T are reported but at atmospheric pressure [33–35]. These studies are limited to a maximum of 2000 K, well below the melting temperature ($T_M = 3160$ K [36]). In an experimental analysis to investigate the elasticity of single-crystal CaO at high-P, Speziale *et al.* [37] involved a combinational study using the Brillouin scattering (BS) and radial x-ray diffraction (RXRD) techniques at RT. However, the study is limited to 30 and 70 GPa for BS and RXRD methods. Theoretical predictions of pressure-dependent ECs (either at $T = 0$ K or RT) for CaO have been made by Karki and Crain [29], Deng *et al.* [30], Jiang *et al.* [11], and Ackland [38]. In a recent study on CaO using DFT-LDA-$\frac{1}{2}$, authors [39] also propose a nearly thermodynamic stable hexagonal phase in addition to conventionally known B1 and B2 phases. Furthermore, the results for the high-P melting curve of CaO are inadequate compared with neighboring isostructural magnesium oxide [40–43]. Wang [44] and Wang *et al.* [45] proposed a model based on the relationship between temperature and thermodynamic properties to predict high-P melting. Sun *et al.* [46] implemented a shell model molecular dynamics (MD) simulation and analyzed the thermal instability to investigate the melting curve of CaO. Restricted either due to experimental limitations or finite-temperature *ab initio* computations, the high-P, T structural phase diagram of lime is incomplete.

Since the pressure and temperature dependence of phonon frequency is known to arise from the non-harmonic character of the interatomic potential, we attempted to incorporate the anharmonicity in our recent work [17] using the lowest-order thermodynamic perturbation theory in conjunction with the DFT-based quasiharmonic (QH) full lattice dynamics. In that study [17], we report comprehensive thermophysical properties, including a bonding scenario in the B1 phase of CaO. Extending the LDA+PAW scheme for the B2 phase, in this paper, we have investigated (P, T) dependence of SPT, high-P melting curve, and various elastic (second-order ECs C_{ij}, bulk modulus B, shear modulus G, and Young's modulus Y), and anisotropic (Zener elastic anisotropy A and Poisson's ratio σ) properties of CaO in both B1 and B2 phases. The present method of computing elastic moduli thus includes the effect of phonon anharmonicity through the correct thermal expansion and therefore goes beyond the conventional QH technique. The isothermal equation of state (EOS), enthalpy H, thermal pressure P_{th}, and thermodynamic Grüneisen parameter γ_{th} are also obtained. To explain the studied phase diagram due to elastic instabilities, the Born elastic criteria for C_{ij} are generalized for arbitrary stress [47–50], the so-called modified Born criterion. Furthermore, as elaborated in the next section, we propose a computational scheme to capture the effect of anharmonicity and structural relaxation to improvise the conventional Lindemann's law of melting [51]. This gives a high-P melting curve in good agreement with classical MD results [46]. By including the pressure dependency of elastic properties, we can show that the solid-solid phase transition is mechanical in a pressure range of 0–200 GPa and temperature up to 3000 K. The shear EC governs the B1-to-B2 SPT, whereas the solid-liquid phase boundary can be treated accurately through the temperature-dependent thermodynamic Grüneisen parameter. The observed peak structured melting curve proposes the insulator-to-metal/semimetal transition ∼200 GPa, which is also discussed.

The rest of the paper is organized as follows. In Sec. II, we give a brief theory and computational strategy for evaluating various thermoelastic properties and the high-P, T phase diagram. Computed results are compared and discussed in Sec. III. The paper is summarized and concluded in the last section.

II. THEORY AND COMPUTATIONAL DETAILS

A. Elastic properties and SPT

In a perfectly harmonic crystal, the ECs are temperature independent. In such a case, they can be conveniently computed using first principles, and their pressure dependence can be derived. However, such static calculations mistreat the effects of temperature and lattice vibrations on elasticity. In our previous work [52], we had evaluated the TDECs of CaO under the quasistatic approximation (QSA) [33,53–57]. TDECs can also be computed within the QHA on a grid of reference geometries. In this method, the phonon dispersion curve (PDC) is computed for a given geometry to evaluate the total Helmholtz free energy as a function of the volume. The TDECs are interpolated and evaluated at equilibrium volume at a given temperature [58,59]. Thus, the QHA scheme, although a very robust technique for computing ECs, requires knowledge of PDC and electronic band structures at several strained geometries, and hence, it is computationally expensive. Instead, we follow a computational scheme where the total Helmholtz free energy is computed after including the T-dependent contribution from phonon anharmonicity [17] (henceforth, we refer to Ref. [17] as Paper I). Computed equilibrium volume at each temperature is an input for the computation of elastic properties. As elaborated in Paper I for the B1 phase of CaO, anharmonicity is significant above RT; an accurate thermal expansion is possible only after including the effect of intrinsic anharmonicity. An accurate volume thermal expansion coefficient of Paper I thus ensures accurate estimates of ECs. In recent work, Levitas [60] derived a general nonlinear theory for elasticity. Although, the effect of temperature and entropy variation is not included in the theoretical framework, the theory incorporates the effect of initial hydrostatic loading effect in various elastic moduli and proposes, as exploited in this paper, that the second-order ECs can be accurately determined from the second-order derivative of volume and temperature-dependent free energy.

According to the elastic theory due to Barron and Klein [49], we can derive the isothermal elastic stiffness coefficients for a strained crystal from the knowledge of total Helmholtz free energy $F(V,T)$ as follows:

$$C_{ij}(V,T) = \frac{1}{V_0(T)}\left[\frac{\partial^2 F(V,T)}{\partial e_i \partial e_j}\right], \tag{1}$$

where $V_0(T)$ is the unit cell equilibrium volume at temperature T, and e_i represents strain along the i direction. The total Helmholtz free energy can be given by

$$F(V,T) = E_C(V) + F^{\mathrm{QH}}(V,T) + F^{\mathrm{An}}(V,T), \tag{2}$$

where $E_C(V)$ is the cohesive energy, $F^{\mathrm{QH}}(V,T)$ is the QH vibrational free energy, and $F^{\mathrm{An}}(V,T)$ is the anharmonic phonon energy. As discussed in detail [17], the PAW pseudopotential [61] was used in the computation. Since high-T thermal assessment for CaO is better estimated by LDA XC functional [17,62], we prefer to use the Perdew-Zunger (LDA) [63] scheme for the XC functional. Recent studies have drawn a similar conclusion for calculating formation energies for alkaline oxides [62]. For both Ca and O, the pseudopotential includes the nonlinear core correction for Ca $3s^2 3p^6 4s^2$ and for O $2s^2 2p^4$ treated as the valence state. We keep the optimized cutoff for the wave function as 140 Ry for the B1 phase and 200 Ry for the B2 phase. The Monkhorst **k**-point grids [64] used are $8\times8\times8$ and $10\times10\times10$, respectively, for the B1 and B2 phases. We evaluated total energy (E) as a function of volume ranging from $0.7V_0$ to $1.25V_0$ in steps of 0.05 a.u. for lattice constant a_0 for both phases. The obtained $E(V)$ at various volumes are then fitted to the third-order Birch-Murnaghan (BM) EOS [65] to obtain an equilibrium lattice constant a_0, equilibrium volume V_0, bulk modulus B_0, and its first-order pressure derivative B_0'. Cohesive energy $E_C(V)$ is calculated using the energy of isolated Ca and O atoms and subtracting the sum of both from E(V). Equilibrium properties for B1 and B2 phases are compared in Table I. The dynamical matrices for each volume are calculated on a $4\times4\times4$ grid in **q**-space using the density functional perturbation theory [66]. The QHA module of the QUANTUM ESPRESSO code [67,68] was employed to derive the PDC and the phonon density of states (DOS) for the entire range of volume. The PDC under zero-pressure conditions and at 67 GPa pressure for B1 and B2 phases are depicted in Figs. 1 and 2, respectively. The knowledge of DOS permits the computation of $F^{\mathrm{QH}}(V,T)$ in Eq. (2). We refer to Paper I for complete details of the anharmonic contribution [third term of Eq. (2)] to the vibrational part of free energy. For the B2 phase, we retain the same anharmonic parameters used in Paper I for the B1 phase within the LDA, table 1 of Paper I. The total free energies as a function of volume but at an

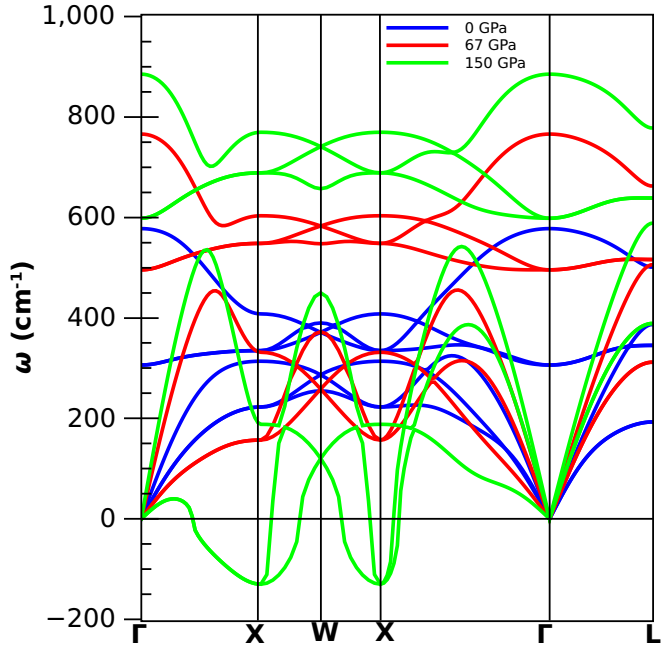

FIG. 1. Phonon dispersion curve of B1 phase.

TABLE I. Ground state properties of B1 and B2 phases.

	This paper		Reported data	
	B1	B2	B1	B2
a_0(Å)	4.7095	2.8488	4.81 [22] Expt. 4.714 [26]	2.907 [23] Expt. 2.85 [26]
B_0 (GPa)	128.51	133.13	115 [22] Expt. 129 [26]	130 [23] Expt. 123 [26]
B_0'	4.36	4.29	4.10 [22] Expt. 4.47 [26]	3.5 [23] Expt.
a_0' (K^{-1})	3.599×10^{-5}			
m	3.5012			

assumed temperature T are fitted to the BM-EOS to obtain an equilibrium $V_0(T)$ and hence the volume thermal expansion coefficient for the B2 phase. In lieu of other data for the B2 phase, we have compared volume expansion coefficients with the one derived within the QH Debye model [69] and with the QSA-based results in Fig. 3. The QH Debye model, which ignores the true phonon DOS, shows an overwhelming rise in expansion, whereas the QSA gives the wrong trend in the computed thermal expansion. Present phonon DOS-based results show a similar trend with and without including the anharmonic contribution. A closer inspection of Fig. 3 also reveals that the anharmonicity reduces the QH expansion values. This comparison justifies and proposes the use of full lattice dynamics in conjunction with an adequate anharmonic contribution for an accurate evaluation of thermal expansion. This is a vital ingredient to this paper, as previous theoretical and experimental studies on a diverse class of materials [70–73] all advocate that the TDECs are predominantly determined by equilibrium volume at a given temperature. In Voigt's notation, for the B1 and B2 phases, the three independent ECs, C_{11}, C_{12}, and C_{44} are computed using THERMO_PW code [74] at each $V_0(T)$. These ECs are further modified to incorporate the hydrostatic pressure term [75] as follows:

$$C_{11}' = C_{11} - P, \tag{3}$$

$$C_{12}' = C_{12} + P, \tag{4}$$

$$C_{44}' = C_{44} - P. \tag{5}$$

Computed TDECs are used to calculate other elastic and anisotropic properties at high-P within the Voigt-Reuss-Hill approximation using standard equations [52,76].

B. High-pressure melting

Melting is a phenomenon in which a solid converts to a liquid above a specific temperature, the melting temperature. However, it changes due to the application of pressure. This first-order phase transition is described by the widely used phenomenological Lindemann [51] criterion (vibrational instability) and the Born [77] criterion (elastic instability). Refined versions of these empirical laws [51,78–80] give the physical explanation of the law and relate the melting

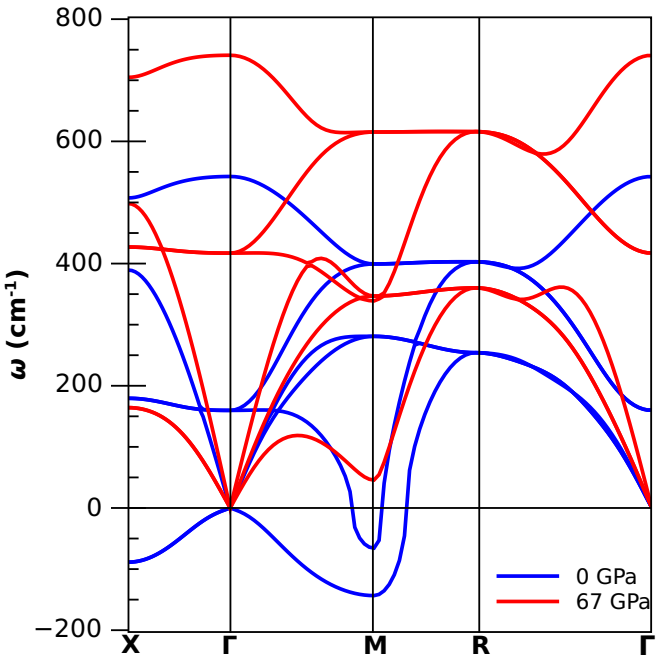

FIG. 2. Phonon dispersion curve of B2 phase.

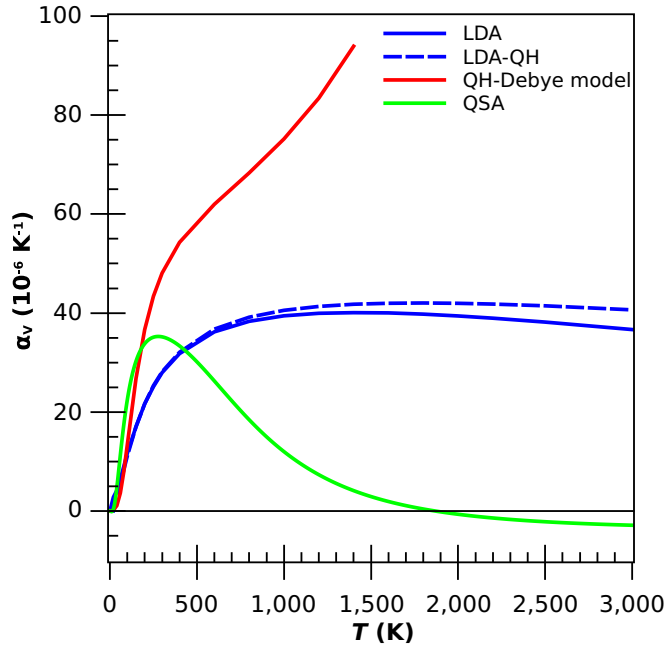

FIG. 3. Volume thermal expansion of B2 phase as a function of temperature.

temperature to entropy [81], thermodynamic Grüneisen parameter [81], anharmonic lattice vibrations [82], phonon DOS [83], and shear modulus [84–87]. Gilvarry [78] has derived the Lindemann melting law in a convenient form using the thermodynamic Grüneisen parameter, which is now generalized to incorporate the explicit effect of temperature:

$$T_M(\eta) = T_M^0 \exp\left\{-\left[2\int_1^{\eta} \frac{\gamma_{\rm th}(\eta, T) - \frac{1}{3}}{\eta} d\eta\right]\right\}. \quad (6)$$

Here, $\eta = \frac{V}{V_0}$ shows the volume fraction, and in this paper, the normal melting point is taken as the experimental value, $T_M^0 = 3160$ K. Equation (6) is found to be satisfactory for producing a low- to moderately high-P melting curve for close-packed fcc metals [88–92] when the QH Grüneisen parameter is considered. At higher pressures, Eq. (6) predicts a steep increase in melting temperature and progressively deviates from the experimental trend, and for more open structures, results are discouraging. The major criticism for this observation is assigned to single-phase computation. The melting process can be attributed to the gradual weakening of intermolecular forces, changes in atomic arrangement, and lattice structure. This assertion was demonstrated on a mathematical framework by Stacey and Irvine [81] and is further extended in this paper to compute the high-P melting curve of CaO up to the pressure of the Earth's LM and outer core. According to Stacey and Irvine [81], Eq. (6) can be derived on a rigorous physical basis by assuming a melting as a four-stage thermodynamic cyclic process involving a melting at constant pressure (isobaric), resolidification at slightly expanded constant volume (isochoric), cooling at reduced pressure (isobaric), and heating at constant volume. The net work done during the cycle is compensated by the heat input (increase in temperature). This mathematical approach derives a correction term to the Clausius-Clapeyron equation as follows (only the most significant correction term is shown):

$$T_M\left(\frac{dT_M}{dP}\right)^{-1} = \frac{L}{\Delta V} \approx \frac{B}{2\gamma_{\rm th}} + \frac{\gamma_{\rm th} C_V T_M}{V}, \quad (7)$$

where C_V is the specific heat at constant volume, and B represents bulk modulus. When solved, Eqs. (6) and (7) are formally equal, but Eq. (7) describes a scope to improvise the melting law quantitatively. The dominating correction term [second term in Eq. (7)] is proportional to $\gamma_{\rm th}$, and it explicitly depends on temperature. At temperatures as high as melting temperature or even higher, C_V can be treated as a constant term. It is to be noted that the inclusion of anharmonicity may lower the value of C_V slightly below the Dulong-Petit value for CaO [17] at ambient pressure, but with pressure, anharmonicity decreases. Under this approximation, it is reasonable to apply correction to the melting slope through variation of $\gamma_{\rm th}$ as a function of temperature. Semi-*ab initio* anharmonic treatment of Paper I allows us to find the explicit temperature dependence of $\gamma_{\rm th}$:

$$\gamma_{\rm th}(V, T) = \gamma_{\rm th}^{\rm QH}(V) - \tfrac{1}{2} m T a(V), \quad (8)$$

where the first term indicates the volume-dependent part of $\gamma_{\rm th}$, whereas the second term depends on temperature. Thus, it is now possible to solve Eq. (6) self-consistently, given the normal melting point, that is, starting from T_M^0, in each step changing $\gamma_{\rm th}$ for a temperature of the last step and recalculating the melting temperature at a given η until the calculation converges. The physical justification of the procedure can be given as follows. If we identify the term $(\frac{\gamma_{\rm th} C_V T_M}{V})$ as internal thermal stress, each iteration relaxes the stress and anneals the system against the increment in temperature. In the theory of Stacey and Irvin [81], this is equivalent to bringing the Gibbs energies of solid and liquid phases close to each other so that the thermal hysteresis in the thermodynamic cycle describing the melting curve reduces. Although the number of self-consistent iterations increases with pressure (smaller η), they are not >5 for pressure as large as 200 GPa.

III. RESULTS AND DISCUSSION

Structural optimization of CaO for B1 and B2 phases has been carried out under the LDA+PAW scheme satisfying the minimum condition for the total energy and forces acting on atoms. Table I shows the ground state properties and the anharmonicity fitting parameters for both phases. Equilibrium lattice constants of both phases agree with the available experimental and theoretical findings. The computed equilibrium lattice constant of the B1 phase varies by 2 and 0.09% with experimental [22] and theoretical [26] findings, respectively, whereas for the B2 phase, the equilibrium lattice constant varies by 2 and 0.04% with experimental [23] and theoretical [26] data, respectively. Equilibrium bulk modulus B_0 and its pressure derivative B_0' for both phases also agree well with the reported findings. The PDC corresponding to computed lattice constants for B1 and B2 phases are presented in Figs. 1 and 2, respectively. The figures also depict that the vibrational spectra of both phases depend strongly on pressure. Most of the vibrational mode frequencies increase with pressure, except for the lowest acoustic branch at the X point and along the $\Gamma \rightarrow X$ direction for the B1 phase. The phonon softening at the X point for the B1 phase exhibits mechanical instability at ∼150 GPa. In contrast, in Fig. 2, for the B2 phase, the negative acoustic phonon frequencies at the X and M points under the equilibrium condition harden with pressure and become positive at ∼67 GPa. Thus, the B2 phase achieves phonon-driven stability at 67 GPa.

Figure 3 shows the temperature dependence of volume thermal expansion (α_V) of the B2 phase. The results are obtained using the same scheme discussed in Paper I employed to compute thermal expansion for the B1 phase [17]. Since no findings for thermal expansion of the B2 phase are available, the present full lattice dynamics-based results are compared with the one based on the QH Debye model [69] and with QSA-based results. QH lattice dynamics uses volume dependence of quasiparticle energies of phonons to compute the approximate free energy. The computed lattice dynamics-based total (including anharmonicity) and QH volume thermal expansion ($\alpha_V^{\rm QH}$) coincide up to 500 K, but dispersion is observed thereafter. This observation suggests the importance of anharmonic contribution >500 K. Total (including anharmonicity) and QH expansion coefficients increase initially and show a slightly decreasing trend beyond 1800 K. The present results with and without anharmonicity deviate significantly compared with both QSA- and QH Debye model-based findings. The low-T deviation is attributed

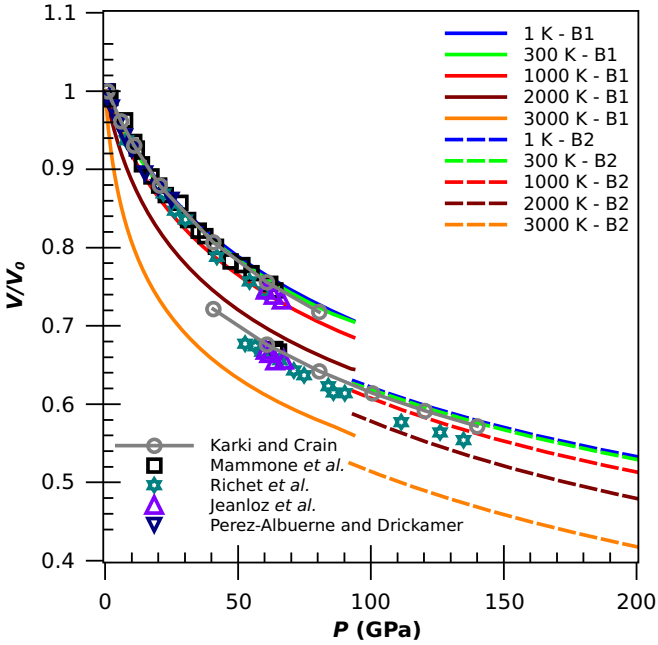

FIG. 4. Equation of state for CaO.

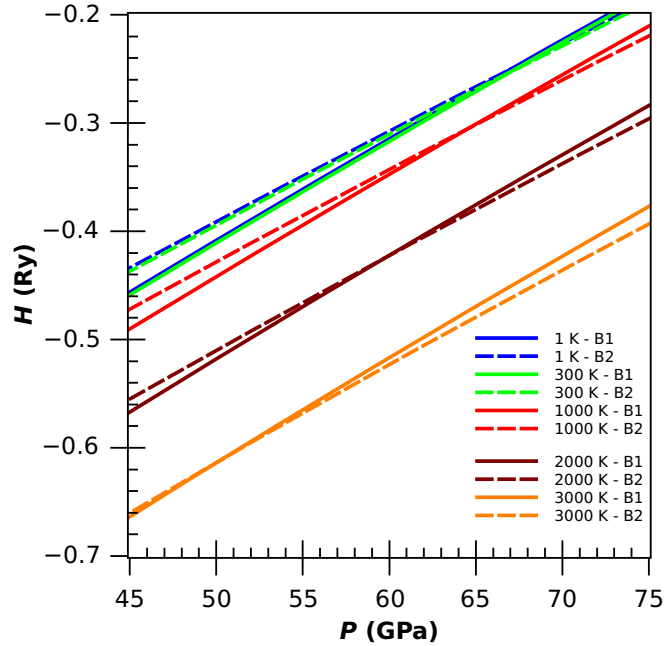

FIG. 5. B1-B2 enthalpy crossing at different temperatures.

to the use of the PAW potential, as discussed thoroughly in Paper I. The QSA-based result shows an increasing trend up to 300 K and then decreases toward a negative value beyond 1800 K. On the other hand, the QH Debye model-based result shows an ever-increasing trend. Overwhelming Debye model-based results and unphysically decreasing results due to QSA advocate the importance of full lattice dynamics results, and we compute all physical properties corresponding to volumes $V_0(T)$ derived using these thermal expansion results.

Figure 4 displays the pressure-volume isotherms for both phases for several temperatures. The $T = 0$ and 300 K EOSs are in good agreement with experimental [20,22,23,93] and theoretical findings [29]. At higher temperatures, the material softens, and the volume fraction (V/V_0) decreases at a constant pressure. To illustrate the phase transition from B1 to B2, we consider the enthalpy of these phases. The enthalpy of B1 and B2 structures as a function of pressure for various isotherms is shown in Fig. 5. At a given pressure, the stable structure is the one whose enthalpy has the lowest value. The transition pressure for the $T = 0$ K lattice is 67 GPa. This agrees with reported results [11]. The B1-B2 enthalpy crossing shifts toward a lower pressure with an increase in temperature and decreases to 50.2 GPa at 3000 K. Corresponding to $T = 0$ K transition pressure, the volume collapses (ΔV_{B1-B2}) by 10.8% and reduces linearly with temperature. At 3000 K, it reduces to 6.2%. However, the transition pressures computed using theoretical methods differ largely from each other as LDA underestimates the transition pressures, while GGA slightly overestimates them.

The mode Grüneisen parameter $\gamma_{n,\vec{q}}(V)$, where $(n, \vec{q})$ is the branch index number, of the B1 phase (Fig. 6) at 0 GPa is positive throughout the first Brillouin zone (BZ) except for small negative values in the vicinity of the Γ point. It is attributed to the numerical nature of the calculation. For the same phase but at 67 GPa, large negative values of the mode Grüneisen parameter show the vibrational instability of the rocksalt structure. The opposite behavior is observed for the B2 phase at both pressures, as shown in Fig. 7. This observation points toward a dynamic nature of phase transition from B1 to B2 at ∼67 GPa.

The elastic properties of the two phases of CaO as a function of pressure are shown in Figs. 8–13. The EC C_{11} represents elasticity in length, and a longitudinal strain can produce a change in C_{11}, whereas C_{12} and C_{44} are related to the elasticity in shape, and hence, a transverse strain changes

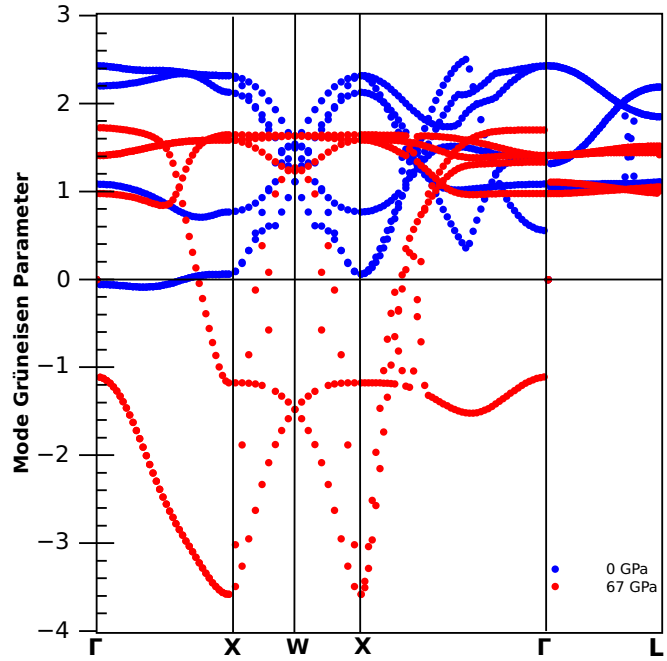

FIG. 6. Mode Grüneisen parameter of B1 phase.

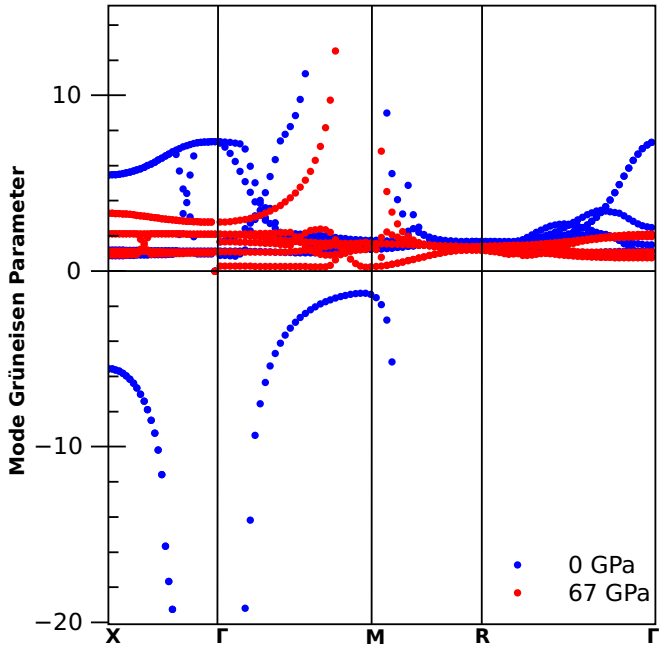

FIG. 7. Mode Grüneisen parameter of B2 phase.

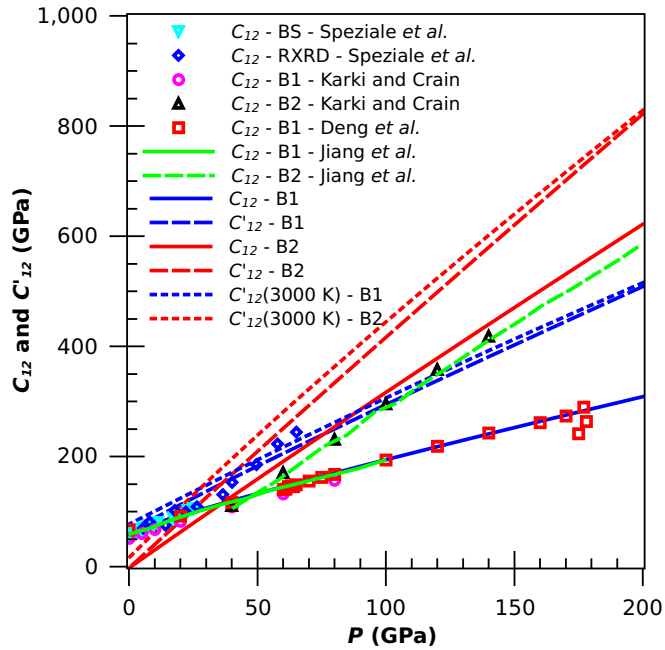

FIG. 9. C_{12} and C'_{12} as a function of pressure.

the shape without the volume change. In the B1 phase, C_{11} varies strongly with pressure compared with C_{12} with a slope of 7.48. For the B2 phase, rather an opposite behavior is observed. The ECs C_{11}, C_{12}, and C_{44} agree well with the experimental [37] and theoretical [11,29,30] findings. Here, C_{44} decreases with pressure for both phases due to the softening of a transverse branch in PDC. For the B2 phase, C_{44} remains positive throughout the examined pressure range. However, it approaches zero value for the B1 phase ∼180 GPa. The Born elastic stability criteria for cubic structure [47,50,58],

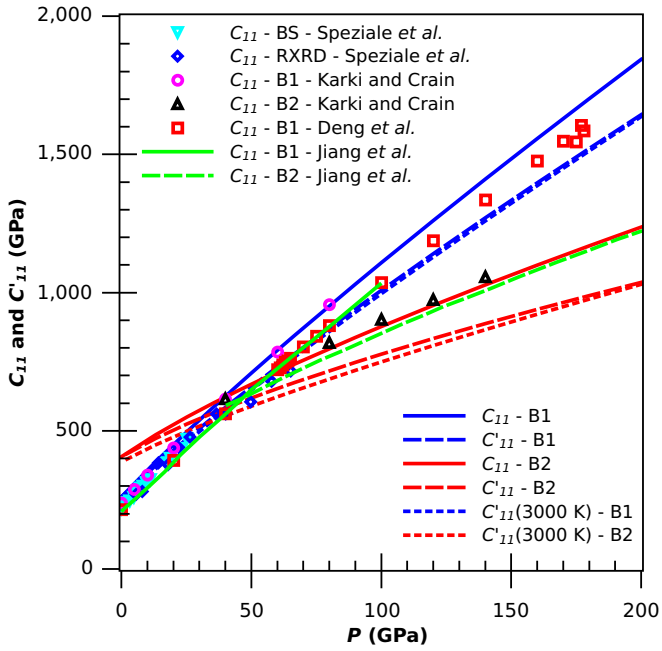

FIG. 8. C_{11} and C'_{11} as a function of pressure.

viz. $(C_{11}+2C_{12}) > 0$, $C_{44} > 0$ and $(C_{11} - C_{12}) > 0$, are connected to the bulk, shear, and tetragonal moduli, respectively. They are commonly referred to as spinodal, shear, and Born criteria. Spinodal and shear conditions are satisfied for both phases, while for the B1 phase, C_{44} becomes negative at 180 GPa, indicating elastic instability. This is manifested as a SPT, but the transition pressure is large compared with the phonon instability; the acoustic transverse branch softens to zero at ∼150 GPa. This apparent conflict can be rectified when the pressure effect is included in ECs. In the strained condition, ECs C_{11}, C_{12}, and C_{44} do not consider the work done against an applied strain. Effective nth-order ECs for hydrostatic pressure consider (i) the change in the free or internal energy of a crystal during the deformation near an initial state at a given pressure and (ii) the work to be done against the pressure by the deformation-induced forces. These pressure-term-included ECs C'_{11}, C'_{12}, and C'_{44} [Eqs. (3)–(5)] can describe the elastic behavior of a crystal with arbitrary loading. The pressure-corrected ECs are also compared in Figs. 8–10. One infers from the figure that C'_{11} is now reduced by 200 GPa at the highest pressure examined in this paper. On the contrary, the pressure term raises C_{12} of both phases by ∼200 GPa. Here, C_{12} and C'_{12} are negative for the B2 phase at zero pressure, indicating an elastically unstable structure. Also, C'_{44} of the B2 phase is positive and increases with pressure, while for the B1 phase, it decreases and becomes negative beyond 60 GPa. This is in excellent agreement with the estimated phase transition pressure (67 GPa) obtained through enthalpy crossing, Fig. 5. When the same computational exercise is carried out for $T = 3000$ K, for the B1 phase, C'_{44} becomes zero at 52 GPa, again in excellent agreement with enthalpy-based phase transition pressure. All original (= pressure uncorrected; C_{ij}) and pressure-corrected (C'_{ij}) ECs for temperature corresponding to 3000 K, except C'_{44}, increase with pressure.

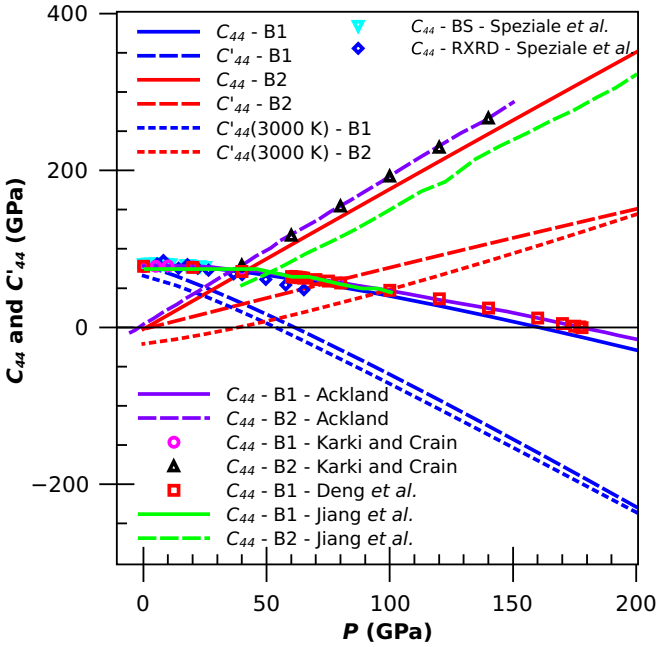

FIG. 10. C_{44} and C'_{44} as a function of pressure.

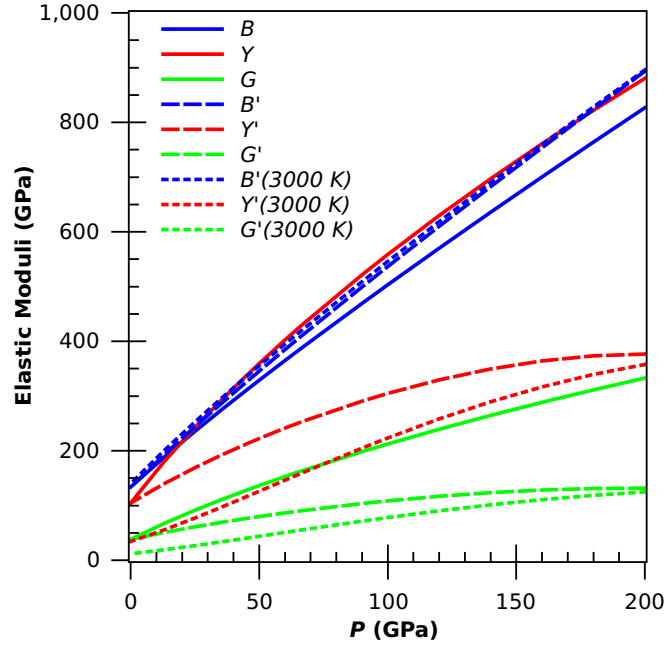

FIG. 12. Elastic moduli of B2 phase as a function of pressure.

Original (= pressure uncorrected) and pressure-corrected elastic properties such as bulk modulus, Young's modulus, and shear modulus for B1 and B2 structures are shown in Figs. 11 and 12, respectively. Here, B' and temperature-dependent B'(3000 K) coincide with each other and remain higher than B by 67 GPa for both structures. Also, Y', G', Y'(3000 K), and G'(3000 K) become negative in the pressure range of 80–100 GPa for the B1 phase, which suggests the instability of the structure. A drastic decrease is observed from Y to Y' and G to G' for both the structures, indicating the sensitivity of these moduli to pressure. The differences between Y' and Y'(3000 K) and for G' and G'(3000 K) decrease with pressure.

The Poisson ratio (σ) and elastic anisotropy factor (A) and their pressure-corrected values (σ' and A') are shown in Fig. 13. Here, σ of the B1 phase increases with pressure, while that of the B2 phase decreases up to 50 GPa and then tends to remain constant. The anisotropy factor for the B1 phase decreases with pressure and becomes negative beyond 180 GPa,

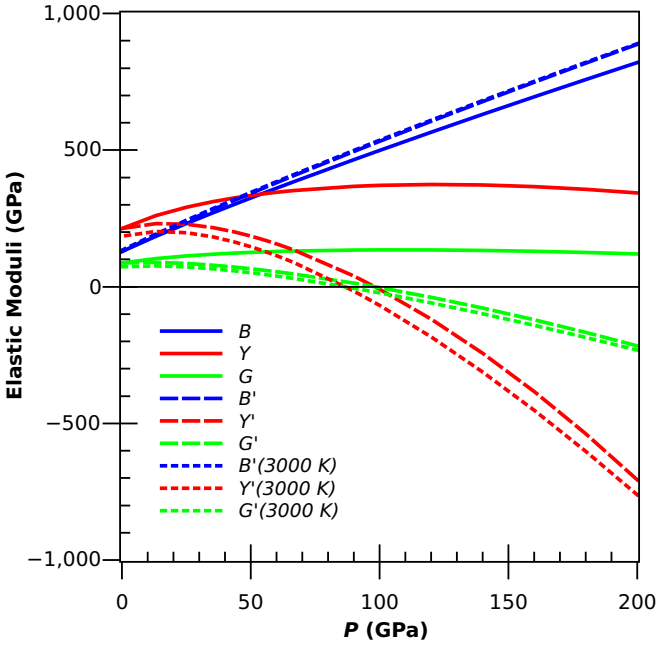

FIG. 11. Elastic moduli of B1 phase as a function of pressure.

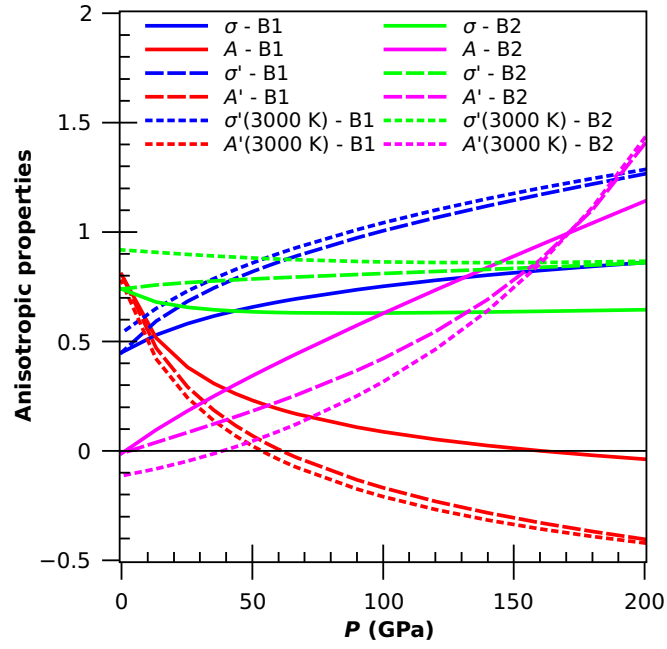

FIG. 13. Poisson ratio and anisotropy factor as a function of pressure.

TABLE II. Elastic and anisotropic properties at the onset of B1-B2 phase transition.

	0 K		3000 K		0 K	3000 K
	B1	B2	B1	B2	Δ_{B1-B2}	
C'_{11} (GPa)	781.03	675.85	769.38	645.91	105.18	123.47
C'_{12}(GPa)	221.13	280.14	232.77	310.08	−59.01	−77.31
C'_{44} (GPa)	−8.66	50.65	−20.31	20.71	−59.31	−41.02
B' (GPa)	407.76	412.04	411.64	422.02	−4.28	−10.38
Y' (GPa)	133.04	253.83	87.12	160.18	−120.79	−73.06
G' (GPa)	46.01	90.82	29.74	55.74	−44.81	−26.00
σ'	0.89	0.79	0.92	0.87	0.10	0.05
A'	−0.03	0.25	−0.07	0.12	−0.28	−0.19

while that due to the B2 phase increases and remains positive throughout the pressure range. Here, σ' of the B1 phase increases with pressure, while that for the B2 phase remains constant with pressure showing an opposite response to external volumetric strain. Also, A' for B1 decreases with pressure and crosses zero at 60 GPa, while for the B2 phase, it remains positive and increases with pressure. Further, σ' (3000 K) follows the same trend as σ' for both phases. Also, A' (3000 K) of the B1 phase decreases and becomes negative at 55 GPa, again indicating instability, while that for the B2 phase remains negative in the initial pressure range showing instability and becomes stable at pressure over 40 GPa. Thus, pressure-corrected elastic moduli and anisotropic parameters also agree with thermodynamic (enthalpy-based) phase transition up to 3000 K.

To investigate the role played by thermoelasticity at the onset of the phase transition, we have tabulated pressure-corrected elastic and anisotropic properties for B1 and B2 phases at $T = 0$ and 3000 K in Table II. An abrupt change is observed in the elastic response at the SPT. For instance, C'_{11} decreases from 781 to 675 GPa; on increasing the temperature from 0 to 3000 K, the difference Δ_{B1-B2} for C'_{11} increases, and it is positive, while the opposite behavior is observed for C'_{12} and C'_{44}, resulting in a negative Δ_{B1-B2}. It is also observed that the higher the temperature, the higher the magnitude of the difference Δ_{B1-B2} for C'_{11} and C'_{12}, but for C'_{44}, it reduces. A similar response is exhibited by B', Y', and G' but with negative Δ_{B1-B2}. The pressure-corrected Poisson ratio σ' stays positive for both phases at both temperatures. Since Poisson's ratio measures the ductility-brittleness of materials, its pressure-corrected value for both phases remains greater than the critical value (0.33), showing that CaO remains ductile. As evidenced by Fig. 13, the anisotropic factor A' drops rapidly with pressure initially for the B1 phase, changes sign to negative ∼50 (43) GPa at $T = 0$ (3000) K, and then decreases more slowly at higher pressures. However, for the B2 phase, it increases, changing the sign from negative to positive ∼4 (44) GPa at $T = 0$ (3000) K, but the difference Δ_{B1-B2} at the SPT remains negative.

The thermal pressure, a measure of the thermoelastic response of the material, as a function of temperature but at equilibrium volume, is shown in Fig. 14. We find that P_{th} increases linearly with temperature >200 K for both phases. Linearity confirms the assertion that cold pressure governs

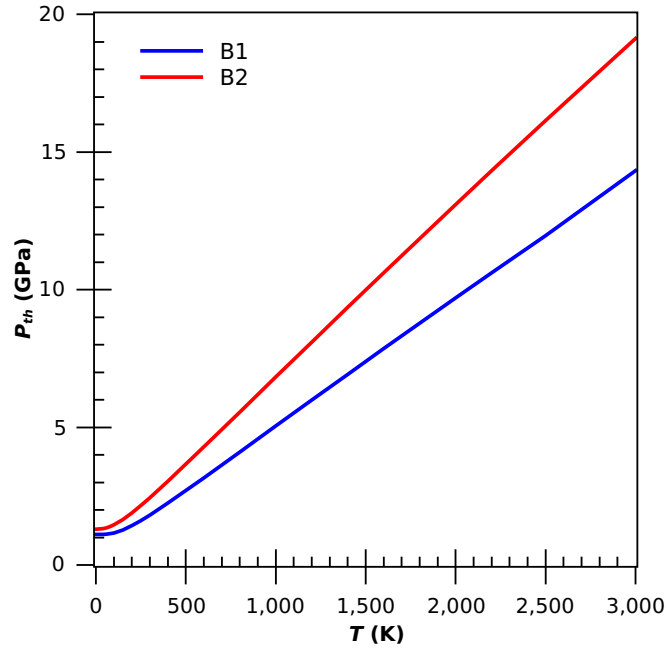

FIG. 14. Thermal pressure as a function of temperature.

the EOS at finite temperatures. However, at low temperatures, the quantum effect gives rise to nonlinearity with almost zero slopes, and the estimated zero-point pressure is ∼1 GPa for both phases. Thermal pressure for the B2 phase remains higher than the B1 phase, which is attributed to the large thermal Grüneisen parameter.

Figure 15 shows the volume variation of thermodynamic $\gamma_{th}(V, T)$, Eq. (8), along the melting curve, and the average mode Grüneisen parameter $\langle\gamma_{n,\vec{q}}(V)\rangle$. Computed results for $\langle\gamma_{n,\vec{q}}(V)\rangle$ at 0 and 67 GPa are shown as symbols, whereas

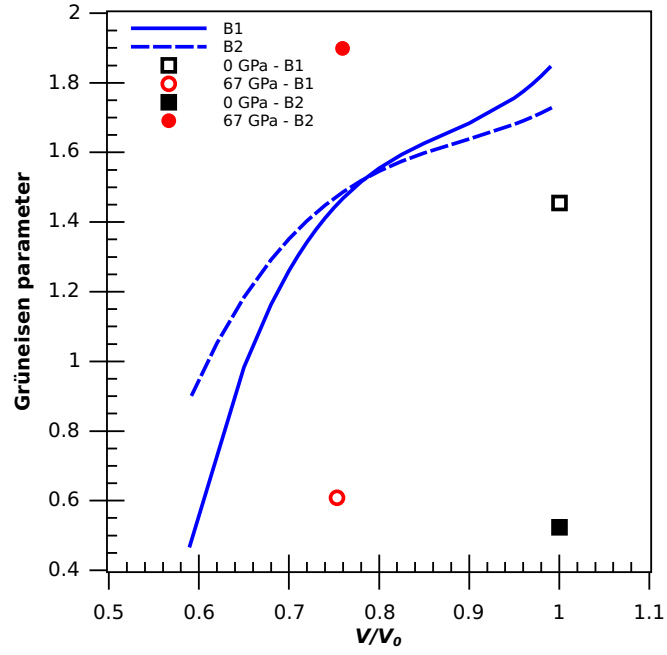

FIG. 15. Grüneisen parameter as a function of volume ratio.

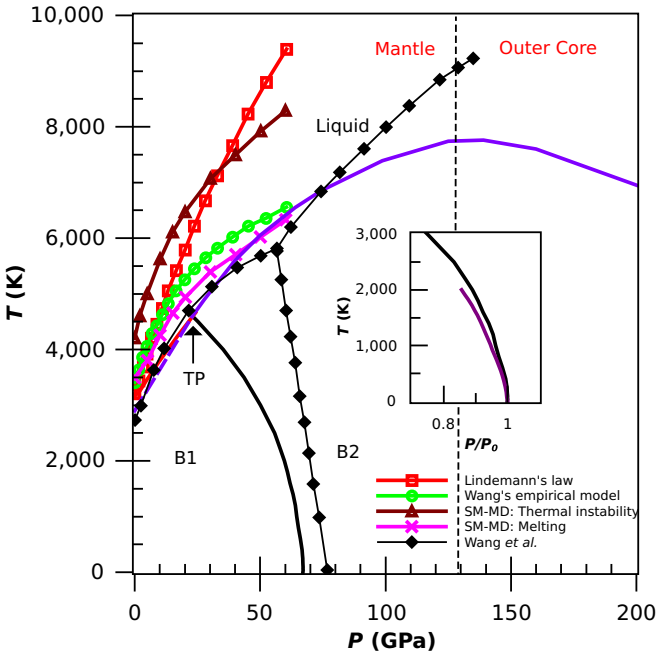

FIG. 16. Structural phase diagram of CaO. Red and purple lines represent the melting curves of B1 and B2 phase, respectively. Dashed line shows the unstable part of the melting curve, and solid lines show the stable part of the phase. Inset shows the comparison of B1-B2 phase diagram with the available data due to Karki and Wentzcovitch [10].

results for the thermodynamic Grüneisen parameter are shown as lines. For the low-P unstable B2 phase, due to cancellation between positive and negative $\gamma_{n,\vec{q}}(V)$, the average value remains very low, but at 67 GPa, it rises to 1.9. However, for both phases, $\gamma_{\rm th}(V,T)$ decreases, more sharply for the B1 phase. Again, due to negative $\gamma_{n,\vec{q}}$ at 67 GPa for the B1 phase, $\langle\gamma_{n,\vec{q}}(V)\rangle$ becomes low.

Figure 16 shows the structural phase diagram of CaO. The present results for finite pressure melting temperatures are in good agreement with the MD simulation results ($T_M^0 = 3200$ K) [46] and Wang's empirical model-based results ($T_M^0 = 3400$ K) [44,45] but deviate significantly from the thermal instability criteria ($T_M^0 = 4200$ K) [46] and with the conventional method that is based on Lindemann's criterion ($T_M^0 = 3200$ K) [46]. The compared melting temperature [46] due to Lindemann's law remains higher by 32% than the computed results at 60 GPa, while it coincides with the MD-based results at the same pressure. The self-consistent computational scheme [Eqs. (6) through (8)], to incorporate the effect of thermal stress into Lindemann's melting law, improves the computed melting curve and brings it in better agreement with other estimates. The variation at 60 GPa of the present data with the results due to Wang's empirical model is 2.8%, and that with the MD results through thermal instability criteria is 23%. All the data, including the present results, agree with the conventional non-iterative Lindemann melting curve only up to 5–6 GPa, and deviation increases rapidly with pressure. Depending on the accurate computation of the reference melting point T_M^0, one can determine the high-P melting curve. Since the anharmonic force law between neighboring atoms, which relates the atomic vibration and the thermal expansion, governs the melting process, the significance of the thermodynamic Grüneisen parameter is apparent in this context. For instance, treating CaO as a weak anharmonic oscillator at high-T, an average vibrational frequency can be written as $\langle\omega_{n,\vec{q}}(V,T)\rangle \approx [\frac{k(V,T)}{m}]^{1/2}$, where $k(V,T)$ refers to the generalized force constant. Through the definition $\langle\gamma_{n,\vec{q}}(V,T)\rangle = -\frac{d\ln\langle\omega_{n,\vec{q}}(V,T)\rangle}{d\ln V}$, if we identify (within the few percent) $\langle\gamma_{n,\vec{q}}(V,T)\rangle$ to be equal to $\gamma_{\rm th}(V,T)$, the temperature-induced vibrational anharmonicity (due to thermal stress, atomic rearrangement, etc.) for interacting ions can be treated through Eq. (8). According to Stacey and Irvine [81], anisochoric heating [constant η in Eq. (6)] leads to the thermal instability which upon relaxing modifies $\gamma_{\rm th}(V,T)$. It is assumed that this modification scales linearly with thermal pressure and can be treated iteratively. Thus, the iterative scheme seems to capture some features of the pre-melting scenario and that of the liquid phase, such as a change in coordination number and possible density crossover at the solid-liquid interface, which in turn modifies the thermal response of the material. The improved high-P melting curve thus corroborates this proposition. Apart from the melting curve, the phase diagram also includes the B1-B2 phase transition, which is compared with the QHA-based result (inset graph) due to Karki and Wentzcovitch [10]. Since present results are incorporated with an anharmonic contribution, a deviation appears between the computed and compared results. The calculated transition pressure decreases with an increase in temperature showing a negative Clapeyron slope $\frac{dP_T}{dT} = -0.0021$ GPa/K. As an important outcome of this paper, we could identify the triple point (TP) for CaO at $(P,T) = (23,\ 4600)$. The TP of CaO lies within the LM. So far, an accurate melting temperature of the B2 phase is not known. To predict the melting temperature of the B2 phase, we have chosen the intersection point of the B1 melting curve and B1-B2 phase transition curve, i.e., $(P,T) =$ (23 GPa, 4600 K), as the reference point. Beyond this point, the B2 phase is stable, and the volume fraction and the explicit T-dependent Grüneisen parameter is known. This information is exploited to deduce the melting curve of the B2 phase using the same method which is employed for the B1 phase. Next, to estimate the correct melting curve below the reference point, and the (theoretical) zero-pressure melting temperature of the B2 phase, we use the fitting procedure as employed in Ref. [94]. The predicted normal melting temperature (2907 K) is compared with the classical MD result (2605 K). Results and methodology are elaborated in detail in the Supplemental Material [95] (see also Refs. [96,97]). Further, very recently, a similar exercise to derive the solid-solid and solid-liquid phase diagrams of CaO was also reported by Wang *et al.* [94]. The authors have proposed interatomic potentials, and performed a classical MD simulation. Their paper reports the structural phase diagram of CaO up to 135 GPa of pressure and temperature up to 9000 K. It is found that the B1-B2 phase transition pressure due to Wang *et al.* [94] remains higher than the experimental pressure range [20–23] with almost constant steep Clapeyron slope as compared with present results and that computed in Ref. [10]. On the other hand, the present first-principles estimate of the B1-B2 transition curve shows the expected general trend, i.e., at higher temperatures, the SPT pressure decreases nonlinearly. Further, the computed

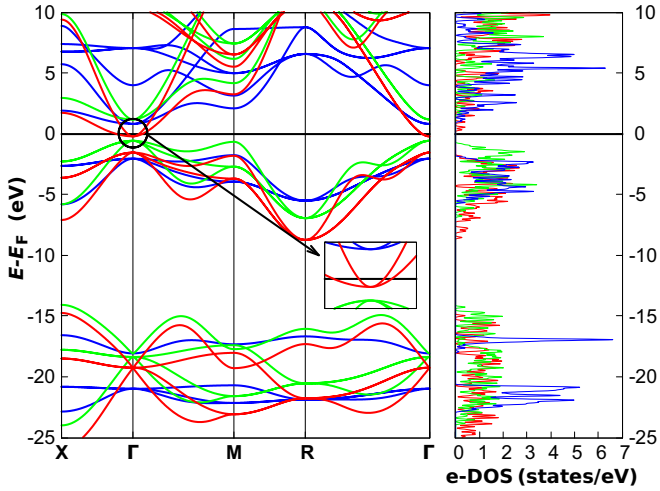

FIG. 17. Electronic band structure (left panel) and electron density of states (e-DOS; right panel) in B2 phase of CaO at 0 GPa (blue), 140 GPa (green), and 200 GPa (red).

Clapeyron slopes $\frac{dP_T}{dT}$ are found to be 0.0160 GPa/K (B1 phase) and 0.0138 GPa/K (B2 phase) at the normal melting temperature, which decrease with pressure. This observation contrasts with the classical MD findings presented in Ref. [94], where the melting curve for the B2 phase increases up to 135 GPa. The relatively low melting slope at moderate pressures seems to be the common characteristic of alkaline earth oxides and perovskites [98]. This study further proposes a negative melting slope >140 GPa with a peak temperature of 7800 K. Such a peak-structured melting curve is previously reported for metals [99] and metallic hydrogen [100]. The unusual melting behavior in these metallic elements was attributed to density crossover between solid and liquid phases either due to the Fermi surface and BZ interaction or to the electronic transition. To examine such a mechanism, we studied electronic band structure and electronic DOS (e-DOS) for the B2 phase at several pressures, Fig. 17. For the B1 phase of CaO, Paper I exemplifies the bonding scenario on the expansion (negative pressure) side. Closer inspection of Fig. 17 indicates that, with pressure, the narrower oxygen $2p$ states (lowest band), oxygen $2s$ states, and calcium $3p$ states get broader, which results in a considerable structure in e-DOS. The conduction states show noticeable variation. The figure also shows the rise in cation energy at the Γ point. Near 200 GPa of pressure, the close proximity of $3d$ states of calcium through plausible hybridization leads to the $s \rightarrow d$ electronic transition and lowers the conduction band to cross the Fermi energy at the BZ center. This insulator-to-metallic/semimetallic phase transition causes the lowering of the melting temperature. The situation is like heavily doped n-type semiconductors [101]. In a recent work [102], the authors have employed the DFT+U scheme under the Hartree-Fock method to demonstrate the existence of pressure-induced localized partially filled electronic states for elemental calcium during the SPT from β-tin to the *Cmmm* phase. The authors attributed such an electride state to a calcium $3d$ state and proposed that the weak Coulomb interaction destabilizes the high-P simple cubic structure. The predicted transition pressure through electronic band structure calculations and the improvised Lindemann's law are different; we attribute this difference to the use of the thermodynamic Grüneisen parameter in Eq. (8), which involves the effect of temperature explicitly through the second term. It is to be noted that the value of $\gamma_{\rm th}$ at the transition point is still positive (= 0.883), indicating a stable B2 phase; however, this nonmetal-to-metal/semimetal (NM-M/SM) transition proposes the different electronic states on either side of the melting maximum. Thus, according to the Clausius-Clapeyron relation, the molar volume on the liquid side is expected to be smaller and more compressible. This proposition, however, invites careful experimental or *ab initio* MD simulation investigation with a higher-order hybridized exchange-correlation function for higher numerical accuracy.

IV. DISCUSSION

ECs are determined from measurements of the sound velocities of acoustic phonons having the frequency range 0.01–0.1 THz. In this range, most materials have a time-dependent relaxation mechanism. Because of their different characteristics concerning temperature, pressure, and frequency, investigations of elastic and anisotropic parameters in combination provide a solid basis for investigating the response of a material to external parameters. According to Landau's theory of the elastic expansion of the Gibbs free energy $G(P, T; \mathcal{Q})$, the thermal agitation acts as an external stress. If we identify the corresponding strain as an order parameter ($\mathcal{Q}$), the crystal will respond to the external stress by adjusting its structural state to the new equilibrium condition. Such a relaxation indicates a reduction in energy. The process of thermally distorting the crystal will have been made slightly easier to appear softer than the crystal, which was not prone to undergoing the SPT. Thus, the thermal stress modifies the curvature of the free energy to bring the new equilibrium state. The 'shape' of the free energy curve is given by the inverse of susceptibility χ, defined as $\chi^{-1} = \frac{\partial^2 G}{\partial \mathcal{Q}^2}$. Since the susceptibility varies in competing phases, an indication of an imminent SPT is often displayed by a decrease in one or more ECs as the transition point is approached. The theory seems to be valid, as Figs. 10, 11, and 13 all advocate that, at the SPT, elastic (C'_{44} and Young's and shear moduli) and anisotropic (A') parameters become zero for the B1 phase. This further confirms that the acoustic transverse phonons determine the symmetry-breaking distortion that leads to zero ECs. The dynamical effects (due to external pressure and temperature) cause additional elastic softening in the vicinity of the transition point, and SPT pressure decreases with temperature. This mechanical (= dynamical) origin of solid-solid phase transition is exemplified in phonon dynamical quantities, like PDC, mode Grüneisen parameter, and enthalpy. Since Lindemann's law is still applicable through the thermal relaxation mechanism, the solid-liquid phase transition is also mechanical. However, at higher pressures, the overlap between s and d orbitals and the proposed electronic transition lowers the conduction band below the Fermi energy at the BZ center. This NM-M/SM phase transition causes a smaller molar volume on the liquid side, which lowers the melting temperature at higher pressure. Since estimated NM-M/SM transition pressure and

temperature falls in the solidus region close to the core-mantle boundary, this is an essential finding because the structural phase transformations are responsible for the discontinuities in the mantle. At the phase boundary, breaking and reconstruction of bonds occur, and unstable phonons and other anharmonic effects may be operative, which are all functions of temperature and pressure. These intrinsic phenomena drive the geochemistry (e.g., formation energy and enthalpy) and, in turn, govern the formation/decomposition of CaPv and the heat transport mechanism.

V. SUMMARY AND CONCLUSIONS

In conjunction with anharmonic lattice contribution, QH lattice dynamics is utilized to compute the volume thermal expansion of the B2 phase of CaO. The structural phase diagram of CaO at high-P, T is computed and compared with the existing data. From the phonon dynamics viewpoint, the B1 phase is stable up to 67 GPa pressure, while the B2 phase is unstable at equilibrium and attains pressure-driven stability at and beyond 67 GPa. The thermodynamic (enthalpy-based) root also advocates the exact inference. The above observation is also supported by the fact that the mode Grüneisen parameter of the B1 phase has negative values >67 GPa. Elastic moduli of both phases are in excellent agreement with the existing experimental and theoretical data. For the B1 phase, when $P < 180$ GPa, C_{ij} are all positive, indicating elastic stability, but beyond 180 GPa, $C_{44} < 0$ shows the instability of the B1 phase. That is, elastically, the B1 phase is stable up to 180 GPa. This apparent conflict can be addressed as follows. The shear instability ($C_{44} = 0$) follows the B1-B2 phase transition along the specific reaction path of the homogeneous deformation, which involves an activation barrier. The large discrepancy between the transition pressures predicted by elastic and thermodynamic criteria can be interpreted as the presence of a substantial activation barrier to a particular transition route [103]. The pressure correction term rectifies it. Here, C'_{44} of the B1 phase softens beyond 10 GPa and drops to zero between 60 and 52 GPa for 0 and 3000 K, respectively. In contrast, for the B2 phase, C'_{44} increases strongly with pressure. The anisotropy of CaO increases with pressure in the B1 structure, drops significantly at the B1-B2 transition point, and decreases gradually. These observations and the discussion in the preceding paragraph confirm that the solid-solid B1-B2 phase transition is dynamical and governed by the softening of shear modes. Further, the proposed self-consistent iterative scheme of relaxing the thermal stress via the temperature-dependent Grüneisen parameter improves the conventional Lindemann's law and gives an accurate melting curve for CaO. We conclude that the proposed iterative scheme thus minimizes the thermal instability along the melting line and brings it in better agreement with the MD simulated melting diagram. This also confirms that the anharmonicity introduced through the perturbative expansion of vibrational free energy in the largest-order of temperature is sufficient for accurate computation of thermal properties. Electronic band structure calculation verifies the predicted negative melting slope >140 GPa. It advocates that the calcium behaves like a transition metal and exhibits the overlap of the empty d band with s orbitals at high pressures and shows electride character. This NM-M/SM phase transition lowers the conduction band energy below the Fermi energy at the Γ point of the BZ. Different electronic states on solid and liquid sides are responsible for lowering the melting temperature with pressure.

ACKNOWLEDGMENTS

The high-performance computing facility at the Department of Physics, Maharaja Krishnakumarsinhji Bhavnagar University, under Grant No. PGP/UGC12/73F/2019 of University Grants Commission, New Delhi, India, is greatly acknowledged. Authors are beholden to the reviewers for suggesting conceptual refining points to improve the manuscript.

[1] D. L. Anderson, *Theory of the Earth* (Blackwell Scientific Publications, Boston, 1989).
[2] Z. Zhang, D.-B. Zhang, K. Onga, A. Hasegawa, K. Ohta, K. Hirose, and R. M. Wentzcovitch, Phys. Rev. B **104**, 184101 (2021).
[3] R. Caracas and R. E. Cohen, Geophys. Res. Lett. **33**, L12S05 (2006).
[4] T. Katsura, H. Yamada, O. Nishikawa, M. Song, A. Kubo, T. Shinmei, S. Yokoshi, Y. Aizawa, T. Yoshino, M. J. Walter *et al.*, J. Geophys. Res. **109**, B02209 (2004).
[5] T. Sun, D.-B. Zhang, and R. M. Wentzcovitch, Phys. Rev. B **89**, 094109 (2014).
[6] P. Ulmer and R. Stalder, Am. Mineral. **86**, 1267 (2001).
[7] S. K. Saxena and G. Shen, J. Geophys. Res. **97**, 19813 (1992).
[8] S. P. Upadhyay and M. Kumar, Phys. Status Solidi B **191**, 299 (1995).
[9] N. A. Dubrovinskaya, L. S. Dubrovinsky, and S. K. Saxena, Geochim. Cosmochim. Acta **61**, 4151 (1997).
[10] B. B. Karki and R. M. Wentzcovitch, Phys. Rev. B **68**, 224304 (2003).
[11] L. Zi-Jiang, Q. Jian-Hong, G. Yuan, C. Qi-Feng, C. Ling-Cang, and Y. Xiang-Dong, Chin. Phys. **16**, 499 (2007).
[12] Z. Fang, J. Appl. Phys. **102**, 013523 (2007).
[13] S. K. Srivastava, P. Sinha, and M. Panwar, Ind. J. Pure Appl. Phys. **47**, 175 (2009).
[14] T. Song, X. W. Sun, R. F. Wang, H. W. Lu, J. H. Tian, and P. Guo, Physica B **406**, 293 (2011).
[15] C. M. S. Alvares, G. Deffrennes, A. Pisch, and N. Jakse, J. Chem. Phys. **152**, 084503 (2020).
[16] A. Erba, M. Shahrokhi, R. Moradian, and R. Dovesi, J. Chem. Phys. **142**, 044114 (2015).
[17] P. Vyas, A. B. Patel, and N. K. Bhatt, Physica B **645**, 414250 (2022).
[18] V. Haigis, M. Salanne, and S. Jahn, Earth Planet. Sci. Lett. **355**, 102 (2012).
[19] H. Hattori and Y. Ono, *Metal Oxides in Heterogeneous Catalysis* (Elsevier, Amsterdam, 2018).

[20] R. Jeanloz and T. Ahrens, Geophys. J. R. Astron. Soc. **62**, 505 (1980).
[21] R. Jeanloz, T. Ahrens, H. K. Mao, and P. M. Bell, Science **206**, 829 (1979).
[22] J. F. Mammone, H. K. Mao, and P. M. Bell, Geophys. Res. Lett. **8**, 140 (1981).
[23] P. Richet, H. K. Mao, and P. M. Bell, J. Geophys. Res. **93**, 15279 (1988).
[24] A. J. Cohen and R. G. Gordon, Phys. Rev. B **14**, 4593 (1976).
[25] M. J. Mehl, R. J. Hemley, and L. L. Boyer, Phys. Rev. B **33**, 8685 (1986).
[26] M. J. Mehl, R. E. Cohen, and H. Krakauer, J. Geophys. Res. **93**, 8009 (1988).
[27] M. S. T. Bukowinski, Geophys. Res. Lett. **12**, 536 (1985).
[28] H. Zhang and M. S. T. Bukowinski, Phys. Rev. B **44**, 2495 (1991).
[29] B. Karki and J. Crain, J. Geophys. Res. **103**, 12405 (1998).
[30] Y. Deng, O. Jia, X. Chen, and J. Zhu, Physica B **392**, 229 (2007).
[31] N. Soga, J. Geophys. Res. **73**, 5385 (1968).
[32] H. Oda, O. L. Anderson, D. G. Isaak, and I. Suzuki, Phys. Chem. Miner. **19**, 96 (1992).
[33] X. Wu, L. Liu, W. Li, R. Wang, and Q. Liu, Comput. Condens. Matter **1**, 38 (2014).
[34] Z. H. Fang, Solid State Sci. **10**, 950 (2008).
[35] S. K. Srivastava, Physica B **387**, 396 (2007).
[36] T. Bgasheva, T. Falyakhov, S. Petukhov, M. Sheindlin, A. Vasin, and P. Vervikishko, J. Am. Ceram. Soc. **104**, 3461 (2021).
[37] S. Speziale, S. R. Shieh, and T. S. Duffy, J. Geophys. Res. **111**, B02203 (2006).
[38] G. Ackland, RIKEN Review No. 29, *Focused on* Large-scale Calculation of Electronic States (2000).
[39] N. Hammou, A. Zaoui, and M. Ferhat, J. Alloys Compd. **815**, 152424 (2020).
[40] T. Kimura, H. Ohfuji, M. Nishi, and T. Irifune, Nat. Commun. **8**, 15735 (2017).
[41] Z. Du and K. K. M. Lee, Geophys. Res. Lett. **41**, 8061 (2014).
[42] Z. J. Liu, X. W. Sun, Q. F. Chen, L. C. Cai, X. M. Tan, and X. D. Yang, Phys. Lett. A **353**, 221 (2006).
[43] D. Alfè, Phys. Rev. Lett. **94**, 235701 (2005).
[44] Z. W. Wang, Phys. Earth Planet. Inter. **115**, 219 (1999).
[45] Z. W. Wang, F. Tutti, and S. K. Saxena, High Temp. High Pressures **31**, 681 (1999).
[46] X. W. Sun, T. Song, Y. D. Chu, Z. J. Liu, Z. R. Zhang, and Q. F. Chen, Solid State Commun. **150**, 1785 (2010).
[47] J. Wang, S. Yip, S. R. Phillpot, and D. Wolf, Phys. Rev. Lett. **71**, 4182 (1993).
[48] J. Wang, J. Li, S. Yip, S. Phillpot, and D. Wolf, Phys. Rev. B **52**, 12627 (1995).
[49] T. H. K. Barron and M. L. Klein, Proc. Phys. Soc. **85**, 523 (1965).
[50] D. C. Wallace, *Thermodynamics of Crystals* (Wiley, New York, 1972).
[51] F. A. Lindemann, Z. Phys. **11**, 609 (1910).
[52] P. Vyas, N. K. Bhatt, and P. R. Vyas, AIP Conf. Proc. **2352**, 020060 (2021).
[53] S. L. Shang, D. E. Kim, C. L. Zacherl, Y. Wang, Y. Du, and Z. K. Liu, J. Appl. Phys. **112**, 053515 (2012).
[54] S. L. Shang, H. Zhang, Y. Wang, and Z. K. Liu, J. Phys.: Condens. Matter **22**, 375403 (2010).
[55] F. Luo, Z. C. Guo, X. L. Zhang, C. Y. Yuan, and L. C. Cai, Philos. Mag. Lett. **95**, 211 (2015).
[56] Z. L. Liu, J. H. Yang, L. C. Cai, F. Q. Jing, and D. Alfè, Phys. Rev. B **83**, 144113 (2011).
[57] Y. Wang, J. J. Wang, H. Zhang, V. R. Manga, S. L. Shang, L. Q. Chen, and Z. K. Liu, J. Phys.: Condens. Matter **22**, 225404 (2010).
[58] M. Born, Math. Proc. Cambridge Philos. Soc. **36**, 160 (1940).
[59] C. Malica and A. D. Corso, J. Appl. Phys. **127**, 245103 (2020).
[60] V. I. Levitas, Phys. Rev. B **104**, 214105 (2021).
[61] G. Kresse and D. Joubert, Phys. Rev. B **59**, 1758 (1999).
[62] J. A. Santana, J. T. Krogel, P. R. C. Kent, and F. A. Reboredo, J. Chem. Phys. **144**, 174707 (2016).
[63] J. P. Perdew and A. Zunger, Phys. Rev. B **23**, 5048 (1981).
[64] H. J. Monkhorst and J. D. Pack, Phys. Rev. B **13**, 5188 (1976).
[65] F. Birch, Phys. Rev. **71**, 809 (1947).
[66] S. Baroni, S. Gironcoli, A. Corso, and P. Giannozzi, Rev. Mod. Phys. **73**, 515 (2001).
[67] P. Giannozzi, S. Baroni, N. Bonini, M. Calandra, R. Car, C. Cavazzoni, D. Ceresoli, G. L. Chiarotti, M. Cococcioni, I. Dabo *et al.*, J. Phys.: Condens. Matter **21**, 395502 (2009).
[68] P. Giannozzi, O. Andreussi, T. Brumme, O. Bunau, M. Buongiorno Nardelli, M. Calandra, R. Car, C. Cavazzoni, D. Ceresoli, M. Cococcioni *et al.*, J. Phys.: Condens. Matter **29**, 465901 (2017).
[69] M. A. Blanco, E. Francisco, and V. Luaña, Comput. Phys. Commun. **158**, 57 (2004).
[70] O. Gülseren and R. E. Cohen, Phys. Rev. B **65**, 064103 (2002).
[71] O. L. Anderson and D. G. Isaak, in *Mineral Physics and Crystallography: A Handbook of Physical Constants*, edited by T. J. Ahrens (The American Geophysical Union, Washington, DC, 1995).
[72] C. A. Swenson, J. Phys. Chem. Solids **29**, 1337 (1968).
[73] E. F. Wasserman, in *Ferromagnetic Materials*, edited by K. H. J. Bushow and E. P. Wohlfarth (Elsevier Science, Amsterdam, 1990).
[74] See, https://dalcorso.github.io/thermo_pw/.
[75] D. C. Wallace, Phys. Rev. **162**, 776 (1967).
[76] R. Hill, Proc. Phys. Soc. A **65**, 349 (1952).
[77] M. Born, J. Chem. Phys. **7**, 591 (1939).
[78] J. J. Gilvarry, Phys. Rev. **102**, 308 (1956).
[79] G. C. Kraut and G. C. Kennedy, Phys. Rev. **151**, 668 (1966).
[80] F. E. Simon and G. Glatzel, Z. Anorg. Allgem. Chem. **178**, 309 (1929).
[81] F. D. Stacey and R. D. Irvine, Aust. J. Phys. **30**, 631 (1977).
[82] A. C. Lawson, Philos. Mag. B **81**, 255 (2001).
[83] S. Luo, A. Strachan, and D. C. Swift, J. Chem. Phys. **122**, 194709 (2005).
[84] L. Burakovsky and D. L. Preston, Solid State Commun., **115**, 341 (2000).
[85] L. Burakovsky and D. L. Preston, Phys. Rev. E **63**, 067402 (2001).
[86] M. H. Nadal and P. L. Poac, J. Appl. Phys. **93**, 2472 (2003).
[87] C. C. Matthai and N. H. March, Phys. Chem. Liq. **44**, 329 (2006).
[88] R. H. Joshi, A. B. Patel, N. K. Bhatt, B. Y. Thakore, and A. R. Jani, AIP Conf. Proc. **1536**, 841 (2013).

[89] R. H. Joshi, N. K. Bhatt, B. Y. Thakore, P. R. Vyas, and A. R. Jani, Comput. Condens. Matter **15**, 79 (2018).
[90] D. R. Gohil, P. N. Vyas, N. K. Bhatt, and P. R. Vyas, KCG E-J. Sci. **18** (2019).
[91] N. K. Bhatt, B. Y. Thakore, P. R. Vyas, and A. R. Jani, Int. J. Thermophys. **31**, 2159 (2010).
[92] C. Bhattacharya and S. V. G. Menon, J. Appl. Phys. **105**, 064907 (2009).
[93] E. A. Perez Albuerne and H. G. Drickamer, J. Chem. Phys **43**, 1381 (1965).
[94] X. Wang, X. Sun, T. Song, J. Tian, and Z. Liu, Vaccum **209**, 111717 (2023).
[95] See Supplemental Material at http://link.aps.org/supplemental/10.1103/PhysRevB.107.014107 for details of the results for zero-pressure thermodynamic properties, a strategy to compute normal melting temperature, and corresponding computational details regarding simulations and convergence threshold .
[96] M. Huggins and J. E. Mayer, J. Chem. Phys. **1**, 643 (1933).
[97] E. Gmelin, Z. Naturforsch. A **24**, 291 (1969).
[98] J. Braithwaite and L. Stixrude, Geophys. Res. Lett. **46**, 2037 (2019).
[99] Q.-J. Hong and A. van de Walle, Phys. Rev. B **100**, 140102(R) (2019).
[100] H. Geng and Q. Wu, Sci. Rep. **6**, 36745 (2016).
[101] W. Sritrakool, H. R. Glyde, and V. Sa-Yakanit, Can. J. Phys. **60**, 373 (1982).
[102] D. Y. Novoselov, D. M. Korotin, A. O. Shorikov, A. R. Oganov, and V. I. Anisimov, J. Phys.: Condens. Matter **32**, 445501 (2020).
[103] B. B. Karki, G. J. Ackland, and J. Crain, J. Phys.: Condens. Matter **9**, 8579 (1997).